Supersolvus Hot Workability and Dynamic Recrystallization in Wrought Co–Al–W-Base Alloys

Katelun Wertz, Donald Weaver, Dongsheng Wen, Michael S. Titus, Rajiv Shivpuri, Stephen R. Niezgoda, Michael J. Mills, and S. Lee Semiatin

Abstract

Gamma-prime strengthened Co–Al–W-based superalloys offer a unique combination of weldability, mechanical strength, creep resistance, and environmental resistance at temperature—leading many to consider the system as an alternative to nickel-base superalloys for future generation turbine engine hardware. However, little information exists regarding the deformation processing required to turn these novel alloys into useable product forms with appropriate microstructure refinement. Supersolvus thermomechanical processing sequences were successfully demonstrated using right-cylindrical upset specimens for two wrought γ'-strengthened cobalt-base superalloys at industrially relevant temperatures and deformation rates. Hot flow behavior and microstructure evolution were quantitatively characterized and compared to available information on a legacy nickel-base system, Waspaloy. Further, density functional theory was used to explore the compositional dependency of the intrinsic material properties influencing single-phase hot working behavior of model Ni–Al binary and Co–Al–W ternary systems. The apparent similarity in the supersolvus thermomechanical processing behavior of Co–Al–W-base systems and their two-phase γ–γ' Ni-base counterparts suggests conventional pathways, models, and equipment may be leveraged to speed transition and implementation of wrought Co–Al–W-base alloys for components where their properties may be advantageous.

Keywords

Cobalt-base • Supersolvus • Wrought processing

Introduction

The two-phase face-centered cubic (FCC) + $L1_2$ Co–Al–W-base alloy system has garnered significant interest over the past few years as the anomalous strengthening peak associated with the γ'–$Co_3(Al,W)$ precipitate phase occurs at a higher absolute temperature than γ'–Ni_3Al [1]. The alloy class has been investigated as a potential alternative to nickel-base superalloys in elevated temperature applications requiring a combination of weldability, mechanical strength, creep resistance, and environmental resistance [2, 3]. The majority of published work on this alloy system has focused on characterization at proposed application temperatures (<1050 °C), with only a few efforts qualitatively assessing the hot workability of polycrystalline Co–Al–W-base alloys under conditions relevant to the industrial thermomechanical processes necessary for component fabrication. Quantitatively defining the material response during hot working is crucial for successful production of wrought metal parts. The assessment of material strength and ductility at near-solvus temperatures provides a critical step for both tooling design and to ensure safe operation of processing equipment prior to production trials. Further, evaluation of microstructure development as a function of thermomechanical processing history allows for control and development of a desirable microstructure—and therefore desirable mechanical and environmental properties—in the final product form.

Early investigations by ATI Specialty Materials established large-deformation upset of homogenized ternary Co–Al–W ingots was feasible on a pilot-scale, particularly when known grain boundary strengtheners such as boron were added to the composition [4, 5]. Further evaluations confirmed recrystallization was achieved in polycrystalline

K. Wertz (✉) · D. Weaver · S. L. Semiatin
Air Force Research Laboratory, Wright-Patterson AFB, Dayton, OH 45431, USA
e-mail: katelun.wertz@us.af.mil

R. Shivpuri · S. R. Niezgoda · M. J. Mills
The Ohio State University, Columbus, OH 43210, USA

D. Wen · M. S. Titus
Purdue University, West Lafayette, IN 47907, USA

S. Tin et al. (eds.), *Superalloys 2020*, The Minerals, Metals & Materials Series,
https://doi.org/10.1007/978-3-030-51834-9_84

Co–Al–W-base alloys under conventional supersolvus rolling conditions [6] and a series of preliminary stress–strain curves were provided for a highly alloyed Co–Al–W at multiple hot working temperatures at one strain rate [7]. While these exploratory studies began to establish the viability of wrought thermomechanical processing of polycrystalline Co–Al–W-base alloys, no quantitative studies have as yet characterized the microstructural evolution during hot work or discussed how the supersolvus behavior compares to that of wrought two-phase γ–γ' nickel-base superalloys.

Results from hot isothermal compression of two highly alloyed wrought Co–Al–W-base alloys have been compared to assess workability of the alloy class. Tests were conducted at supersolvus temperatures (up to 150 °C above solvus) and deformation rates pertinent to industrial wrought processes. Flow behavior and microstructural evolution of Co–9Al–9W–2Ta and Co–10Al–4W–25Ni–2Ta–2Ti (at.%) were evaluated as a function of temperature, strain, and applied strain rate. The mechanisms and kinetics controlling dynamic recrystallization were established for the Co-base alloys and contrasted to available literature on a common contemporary Ni-base superalloy, Waspaloy.

Materials and Experimental Methods

Starting Material and Supersolvus Compression Test Parameters

Two cobalt-base superalloys were chosen for comparison (compositions provided in atomic percent): Co–9Al–9W–2Ta for its ubiquity in the pre-existing literature and Co–10Al–4W–25Ni–2Ta–2Ti as a higher solvus wrought variant [8, 9]. The γ' solvus temperatures $T_{\gamma'}$ were experimentally established as 1080 and 1132 °C for each alloy, respectively, with the equilibrium γ' fraction at 850 °C found to be approximately 58–60 vol.% for both alloys. Pilot-scale ingots were produced by ATI Specialty Materials via vacuum induction melting and refined using vacuum arc remelting (VIM + VAR); thermal homogenization, conversion via extrusion, and supersolvus recrystallization heat treatment were conducted on the as-cast materials to produce an equiaxed starting grain structure for the test material. Specific processing conditions are provided in Table 1, along with details of the compression tests conducted, for each composition. It should be noted that although 0.02 wt% B was added during the melting of each alloy, the boron levels were below detection limits in homogenized specimens assessed using inductively coupled plasma (ICP) spectroscopy. It is unclear why there was an apparent loss of B. No borides were observed in the cross-sections either, so it was assumed that *intentional* grain boundary pinning or strengthening mechanisms were not present in either of the assessed materials. However, in the Co–9Al–9W–2Ta material, a non-trivial 1–3% volume fraction of intermetallic phase precipitates persisted from the as-cast state into the wrought material; the phase was suspected to be primary μ-Co_7W_6 formed in interdendritic regions during solidification [8]. No such third-phase was observed in the Co–10Al–4W–25Ni–2Ta–2Ti material. The unoptimized composition and processing efforts resulted in starting material with a larger mean grain size than typically associated with well-optimized wrought structures, but equiaxed nature.

Upset testing was conducted for both Co–Al–W-base compositions using right-cylinder samples at temperatures and strain rates relevant to supersolvus wrought processing practices (Table 1). The specimen cylinders were aligned such that the compression axis paralleled both the as-cast ingot axis and the extrusion axis. The specimens were centerless ground, compression faces surfaced, and edges chamfered prior to testing. Boron nitride lubricated specimens were compressed using induction-heated platens mounted in a servo-hydraulic frame. Traditional borosilicate-based glass lubricants reacted strongly with the cobalt alloy in air at hot working temperatures, so boron nitride was employed instead. Specimens underwent either a nominal 1.5:1 or 3:1 reduction; however, system deflection and thermal expansion resulted in actual reductions of 1.46:1 or 2.65:1, respectively.

The temperature variation within a compression specimen during testing was evaluated by embedding a thermocouple at both the center of a specimen and along three locations at the specimen surface (top, centerline, and bottom); the difference between all four locations was within 2 °C after heat ramp and 30 s soak at 1182 °C. At the end of a test, compression specimens were water quenched within 1.5 s, achieving a cooling rate of approximately −200 °C s^{-1}. The recorded load-deflection data was corrected for system compliance and transformed to true stress–true strain curves using a constant volume assumption. Further corrections to account for interfacial friction and deformation heating effects were implemented as detailed in [9] such that the results can be used to interpret the isothermal flow behavior of the materials.

Metallography and Characterization

Traditional metallography techniques were used to prepare samples for observation. Bulk specimens were mechanically ground, lapped, and polished; final polishing was conducted using 0.05 μm diamond to avoid etching artifacts observed when finishing Co-base alloys with colloidal silica. The magnetic effects of as-hot worked bulk specimens were found to be strong enough to influence electron microscopy

Table 1 Processing and upset test conditions for the two Co–Al–W-base alloys chosen for evaluation

Material		
Composition (at.%)	Co–9Al–9W–2Ta	Co–10Al–4W–25Ni–2Ta–2Ti
γ' solvus temperature ($T_{\gamma'}$) (°C)	1080	1137
Ingot production		
Primary melt + refinement	VIM + VAR	
Ingot diameter (mm)	200	92
Ingot mass (kg)	125	21
Ingot homogenization		
Environment	99.999% Argon	
Temperature (°C)	1232	
Soak time (h)	96	48
Quench	Controlled furnace cool (−2 °C min^{-1})	
Primary conversion		
Deformation path	Direct extrusion	
Preheat temp.; time (°C; h)	1204; 1.5	1232; 1.5
Reduction	6:1	
Extrusion rate (m min^{-1})	1.5	1.9
Quench	Vermiculite cooled	
Recrystallization heat treatment		
Temperature (°C)	1204	1157
Soak time (h)	1.0	
Quench	Air cooled	
Mean grain size, circle equivalent diameter (μm)	90 ± 35	225 ± 169
Supersolvus compression testing		
Specimen size: OD × h (mm)	20 × 30	9 × 13.5
Test temp. (Δ Over $T_{\gamma'}$) (°C)	1149 (69), 1204 (124)	1157 (20), 1182 (45)
Compression rate (s^{-1})	0.01, 0.1, 1.0	
Reduction	3:1	1.5:1, 3:1
Quench	Water quench	

Further details can be found in [8, 9]

characterization techniques; therefore, before characterization, the microstructure evaluation specimens were thinly sectioned and demagnetized using an alternating current coil. Conventional TEM foils were prepared by coring 3 mm disks from thin slices cut from the centerline of the compressed-and-quenched samples, parallel to the compression axis. Foils were electro-polished approximately 5 min at −25 °C at 16 V, 10 mA using 56% methanol, 38% 2-butoxyethanol, and 6% $HClO_4$ by volume.

For microstructural evaluation and defect analysis at high magnifications, bright field transmission electron microscopy (TEM) was conducted using a FEI/Phillips CM-200 operated at 200 kV. All of the grain size statistics and texture data presented in the following sections were obtained via electron backscatter diffraction (EBSD). Recrystallized grains were identified simply by partitioning the EBSD data based on the magnitude of rotation observed within a given grain. Grains with more than 2.5% (absolute) grain orientation spread were considered unrecrystallized. High angle grain boundaries were defined as exceeding 15° misorientation. The fraction of recrystallized material was determined by comparing the area of recrystallized grains to that of the total 2D EBSD scan area. Both Σ3 (60° about ⟨111⟩) and Σ9 (38.9° about ⟨110⟩) twins were ignored from the grain size calculations per ASTM International Research Report E04-1008. Additionally, grains sectioned by the edge of the scan field were considered incomplete representations and were removed from further analyses.

Estimations of Stacking Fault Energy (Density Functional Theory: Axial Nearest Neighbor Ising Model)

To provide additional context when comparing Ni–Al-base and Co–Al–W-base supersolvus behavior, the stacking fault energies of model Co–Ni binary and Co–Ni–Al ternary compositions were evaluated using the axial nearest neighbor Ising model (ANNI) [10]. The energy difference between the hexagonal close packed (HCP) and FCC phases with the same composition gives rise to the first-order approximation of the stacking fault energy (SFE):

$$\mathrm{SFE} = \frac{2(E_{\mathrm{HCP}} - E_{\mathrm{FCC}})}{A_{\{111\}}}$$

in which E_{HCP}, and E_{FCC} are energies of HCP and FCC structures and $A_{\{111\}}$ is known as the area of the {111} glide plane. This model or the higher-order versions have been used for previous studies on various Ni- and Co-base alloys to investigate planar fault energies [11–15].

To mimic the disordered solid solution pertinent to supersolvus conditions, special quasi-random structure (SQS) supercells were employed to construct the FCC and HCP phases [16]. To evaluate the SFE as a function of Co concentration, the Co–Ni alloys we investigated in this study included: Co_{100}, $Co_{70}Ni_{30}$, $Co_{50}Ni_{50}$, $Co_{30}Ni_{70}$, and Ni_{100}. The influence of 10 at.% Al addition, was evaluated using: $Co_{90}Al_{10}$, $Co_{63}Ni_{27}Al_{10}$, $Co_{45}Ni_{45}Al_{10}$, $Co_{27}Ni_{63}Al_{10}$, and $Ni_{90}Al_{10}$. With the exception of the pure Co and pure Ni calculations, 60-atom SQS supercells were generated for both the FCC and HCP structures of the above-mentioned alloys using Alloy Theoretic Automated Toolkit (ATAT) [17]. The same supercell structures could be employed for multiple evaluations simply by exchanging the element on the lattice sites (e.g., $Co_{90}Al_{10}$, and $Ni_{90}Al_{10}$; $Co_{70}Ni_{30}$ and $Co_{30}Ni_{70}$; or $Co_{63}Ni_{27}Al_{10}$, $Co_{27}Ni_{63}Al_{10}$; etc.) A complete list of specific SQS supercells with lattice site labels is available on request. Randomness of the SQSs was guaranteed through the use of correlation functions [16], which were enumerated up to the 4th nearest neighbor pairs, the 2nd nearest neighbor triplets, and the 2nd nearest neighbor quadruplets. The majority of the SQS supercell correlation function terms were within ±0.01 of the corresponding ideal solid solutions of a given composition.

Density functional theory calculations were carried out with the Vienna Ab initio Simulation Package (VASP) [18, 19]. The projector augmented-wave method was used to describe the ion–electron interactions and standard pseudopotentials were selected for all elements [20]. The electron exchange-correlation was approximated by the generalized gradient approximation of Perdew, Burke, and Ernzehof [21]. All degrees of freedom were allowed to relax during optimization, with an energy cutoff of 450 eV. K-point meshes were calculated by the Monkhorst–Pack method [22] to guarantee 21 × 21 × 21 evenly spaced k-points in the reciprocal space for primitive cells of both the FCC and HCP structures. A first-order Methfessel–Paxton method [23] was used to describe the partial occupancies with a width of 0.2 eV during relaxation. All calculations were spin-polarized with the initial magnetic moments for Co, Ni, and Al atoms established as 2, 1, and 0 Bohr magneton, respectively. The total energy of each supercell was assessed through a static run using the tetrahedron method with Blöchl corrections when structural relaxations converged within three steps.

The intrinsic stacking fault energies of select compositions were assessed at finite temperatures by incorporating harmonic vibrational approximations [24, 25]:

$$\begin{aligned}\gamma_{\mathrm{SFE}}(T) &= \frac{2(G_{\mathrm{HCP}}(T) - G_{\mathrm{FCC}}(T))}{A_{\{111\}}} \\ &= \frac{2\left(E_{\mathrm{HCP}} + F^{h}_{\mathrm{HCP}}(T) - E_{\mathrm{FCC}} + F^{h}_{\mathrm{FCC}}(T)\right)}{A_{\{111\}}}\end{aligned}$$

where $G_{\mathrm{HCP}}(T)$ and $G_{\mathrm{FCC}}(T)$ represent the Gibbs energies at temperature T for each phase—as modeled with both a nonharmonic E and a harmonic $F^{h}(T)$ free energy contribution. Vibrational and volumetric effects due to the quasi-harmonic approximations were not considered in this initial analysis. Harmonic free energies were calculated through finite displacement method using phonopy [24, 25]. VASP settings were consistent with the static runs, with the exception of a high convergence criterion of 10^{-8} eV for the Hessian matrix was employed. To reduce the computational cost of the phonon calculations, 30-atom (rather than 60-atom) supercells were constructed for HCP and FCC structures. For each reciprocal primitive cell, a k-point grid of 31 × 31 × 31 was used to integrate the phonon dispersion curve across the first Brillouin Zone.

Results

Extent of Dynamic Recrystallization

Dynamic recrystallization (DRX) was observed at the center of each upset specimen under all test temperatures and strain rates evaluated; further, all test conditions produced sound material with no observed cracking despite the lack of apparent grain boundary strengtheners (Fig. 1). Nucleation of new grains occurred preferentially along pre-existing grain boundaries (or in the case of Co–9Al–9W–2Ta at third-phase particles), presenting as the classic “necklace” structure that results when the initial grain size is significantly larger than the recrystallized grain size. Increased test

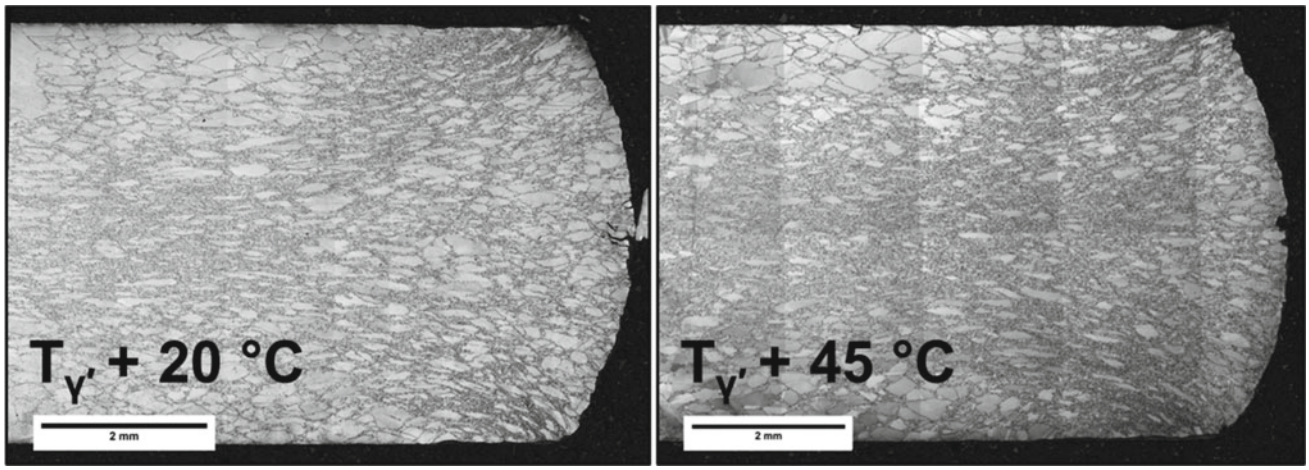

Fig. 1 Example micrographs of sectioned compressed-and-quenched Co–10Al–4W–25Ni–2Ta–2Ti specimens upset 3:1 at 0.01 s^{-1}. Samples were metallographically prepared and etched with a macro cobalt etchant (by volume: 0.25 water, 0.25 nitric acid, and 0.5 hydrochloric acid)

temperatures resulted in a higher fraction of transformed material with larger recrystallized grains observed for a given strain rate. At each test temperature the microstructure was noticeably less recrystallized at the intermediate strain rate than at either the slower or faster applied rates, producing a saddle-shape dependency of dynamically recrystallized fraction X_v on strain rate at all temperatures (Fig. 2). Similar DRX dependency on strain rate has been observed in nickel-base superalloys, such as Alloy 718, where it was suggested the decreased fraction recrystallization at an intermediate strain rate was due to relatively low combined dynamic and post-dynamic recrystallization kinetics, the latter being dependent on the time between the cessation of deformation and the water quench [26]. While not shown, a similar saddle-shape dependency between recrystallized grain size and strain rate was seen and attributed to meta- or post-dynamic growth prior to quench.

Comparison of the extent of DRX after upset in Co–9Al–9W–2Ta and Co–10Al–4W–25Ni–2Ta–2Ti indicate the recrystallization kinetics of the cobalt-base superalloys bound that of similar grain size Waspaloy (100 µm mean) at similar temperature differences above solvus (Fig. 3) [27]. While the recrystallization curve for Co–9Al–9W–2Ta indicated faster transformation kinetics than Waspaloy, the presence of undesirable μ-Co_7W_6 phase likely provided additional recrystallization nuclei sites via particle-stimulated nucleation. Considerably larger strains were necessary to reach 50% recrystallization in the Co–10Al–4W–25Ni–2Ta–2Ti alloy as compared to Waspaloy (i.e., $\varepsilon = 1.15$ vs. $\varepsilon = 0.75$, respectively, at similar temperature deltas above solvus).

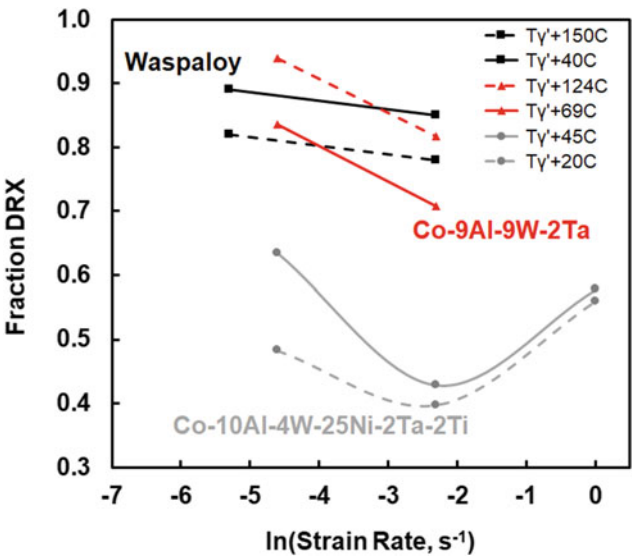

Fig. 2 Comparison of fraction recrystallized as a function of strain rate for coarse-grain wrought Co–9Al–9W-2Ta, Co–10Al–4W–25Ni–2Ta–2Ti, and 100 µm mean grain size wrought Waspaloy product [27]

Supersolvus Hot Work Flow Behavior

The isothermal flow curves obtained via hot compression exhibited classic hot deformation behavior across all test temperatures and strain rates (Fig. 4). Almost all of the test conditions exhibited a distinct upper yield peak, presumably due to the initial low dislocation density present in the slow-cooled extruded and annealed starting material [28]. At low strains, the increased flow stress was dominated by work

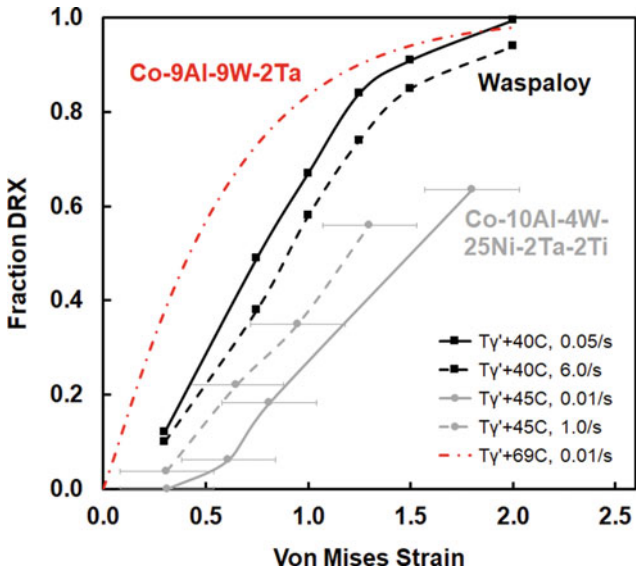

Fig. 3 Dependence of fraction of DRX on local von Mises strain at supersolvus temperatures. Results for Co–9Al–9W–2Ta and Co–10Al–4W–25Ni–2Ta–2Ti are compared to similar grain size Waspaloy across similar test temperatures and strain rates [27]

hardening as dislocations multiplied and interacted with increased deformation; it is important to recognize that some dislocation annihilation also occurred at this stage, but that the flow behavior is largely dictated by strain hardening. The material strength continued to increase until a peak plastic strength was reached, signaling the strain at which restorative mechanisms—dynamic recovery and/or dynamic recrystallization—began to noticeably anneal the structure. The term "dynamic restoration" will be used subsequently to describe the flow softening resulting from the combination of these two restorative processes during loading. Both the rate at which work hardening occurred for given strain and the strain at which the peak plastic strength was observed increased with decreasing temperature and increasing strain rate, similar to other FCC materials [29]. The initiation of DRX is generally accepted to occur at 5/6 of the strain associated with peak strength, but the impact of material softening is low at the very early stages of transformation [30–32]. With increased deformation past the peak strength, a balance begins to develop between the dynamic hardening and restoration mechanism; the magnitude of softening at higher strains was minimal and a saturation strength was reached where dynamic recovery and recrystallization roughly compensate the hardening effects with increased deformation.

At temperatures 45–50 °C above $T_{\gamma'}$, the strain rate sensitivity m for both Co–Al–W-base alloys was relatively low and independent of strain [8, 9]. For Co–9Al–9W–2Ta, an average m = 0.15 was assessed at plastic strains between 0.3 and 1.3; for Co–10Al–4W–25Ni–2Ta–2Ti, m was found to be 0.19 across the same strains. Although using independent upset tests to calculate strain rate sensitivity was not preferred since the dislocation structure differs between test conditions, the supersolvus values calculated here match well with unpublished jump rate tests on homogenized ingot material where the microstructure was constant at deformation rate changes. The low m suggests conventional dislocation-based mechanisms control the hot work processes for these large grain specimens, rather than grain boundary sliding or other superplastic-like behaviors.

In order to compare the hot deformation response of the cobalt-base alloys featured here to other alloy families, the apparent activation energy for dynamic restoration (i.e., dynamic recovery *and* dynamic recrystallization) was estimated using a constitutive relationship between the peak plastic strength σ_p obtained during uniaxial, isothermal hot work, and the Zener–Hollomon parameter Z describing the testing conditions [30]:

$$Z = A\sigma_p^{\frac{1}{m}}$$

$$Z = \dot{\varepsilon}\exp\left(\frac{Q_d}{RT}\right)$$

where A is a material-dependent fitting parameter assumed constant during hot working conditions and m is the strain rate sensitivity of the material. The Zener–Hollomon parameter Z is often employed as a single descriptor for given set of applied test conditions, effectively a temperature-dependent strain rate, dependent only on the applied strain rate $\dot{\varepsilon}$, the deformation temperature T, the universal gas constant R, and the apparent activation energy for dynamic restoration Q_d. By recognizing Z is constant for a given σ_p, Q_d can be estimated as follows:

$$Q_d = R\left(\frac{\partial \ln \dot{\varepsilon}}{\partial \ln \sigma}\right)\left(\frac{\partial \ln \sigma}{\partial (1/T)}\right)$$

The apparent dynamic restoration activation energy can then be estimated as 462 kJ mol^{-1} for Co–9Al–9W–2Ta and 490 kJ mol^{-1} for Co–10Al–4W–25Ni–2Ta–2Ti under supersolvus conditions. The available data was too sparse to provide error estimates given the methodology used for calculation; however, the apparent activation energy for hot deformation agreed well with published measurements on wrought nickel-base superalloy systems (Table 2). The values measured for the cobalt alloys investigated here were, at most, approximately 5–8% higher than observed in nickel-base superalloys for both single-phase and two-phase regions. This methodology provides an "engineering" estimate for an apparent activation energy that encompasses multiple physical mechanisms and does not distinguish

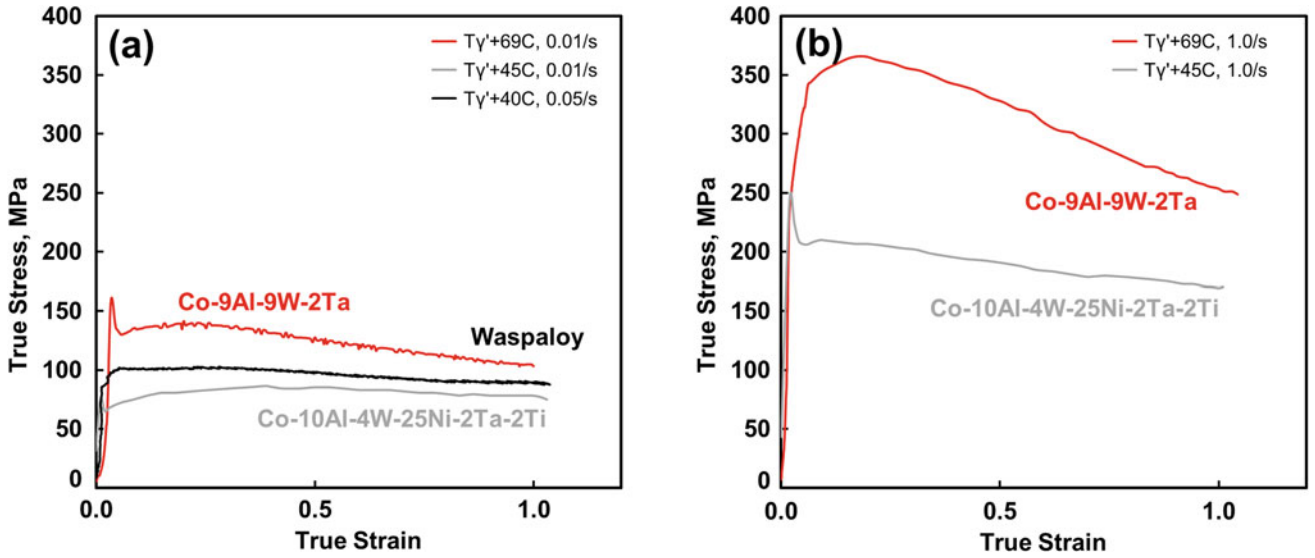

Fig. 4 Comparison of isothermal supersolvus flow curves for wrought polycrystalline Co–9Al–9W–2Ta and Co–10Al–4W–25Ni–2Ta–2Ti as established from right-cylindrical upset tests at conditions listed in legend [9, 33]. Isothermal Waspaloy data from [34]

Table 2 Material comparison of apparent activation energy required for steady-state hot deformation

Element/alloy	Q_d (kJ mol^{-1})	Source
L-605 (solid-solution co-base alloy)	87	[38]
Elemental Co, unknown purity	254	[38]
Elemental Ni, unknown purity	274	[39]
Waspaloy, supersolvus	468	[34]
Co–9Al–9W–2Ta (at.%)	462	[8]
Co–10Al–4W–25Ni–2Ta–2Ti (at.%)	490	[9]

between them or other microstructural influences such as grain morphology, texture, or the presence of $L1_2$ precipitates. Hardening and annealing occur simultaneously during dynamic loading once the peak plastic stress has been reached, so the calculation here incorporates the mechanisms of both: dislocation generation, dislocation climb and glide, dislocation annihilation, dynamic recovery, DRX, grain boundary migration, etc. It is unclear whether this small difference in apparent activation energies between Ni- and Co-base alloys is a result of this generality, differences in calculations between manuscripts, or indicative of mechanistic differences between the Ni- and Co-base alloys.

Experimentally determined apparent activation energies are often compared to physical activation energies in an attempt to interpret which mechanism is rate-controlling. However, in instances where DRX occurs, interpretation is difficult as the apparent activation energy can be considered an aggregate of the energies for soft, recrystallized material *and* hard, unrecrystallized regions, such that energy calculations may be considerably higher than any given physical mechanism [35]. For reference, the magnitude of the dynamic restoration activation energy measured here is considerably larger than for Co self-diffusion at hot working temperatures ($Q_{Co}^{Co} = 260$ kJ mol^{-1} [36]) or interdiffusion of a solute. Tungsten has the largest activation energy of the alloying elements for interdiffusion in FCC cobalt, $Q_w^{Co} = 289.2 \pm 7.0$ kJmol^{-1} [37].

Dynamic Restoration Kinetics

An adaptation of the Johnson–Mehl–Avrami–Kolmogorov (JMAK) relationship can be used to provide an initial, phenomenological estimate of DRX kinetics. The time parameter in the classic JMAK transformation equation can be replaced by strain using the relation $\varepsilon = \dot{\varepsilon}t$, such that the fraction of dynamically recrystallized material X_v becomes a function of the imparted strain ε, the critical strain at which DRX initiates ε_c (5/6 of the strain at peak plastic stress), the strain to reach 50% fraction transformed $\varepsilon_{0.5}$, and two fitting parameters k and n [31]:

$$X_v = 1 - \exp\left(-k\left(\frac{\varepsilon - \varepsilon_c}{\varepsilon_{0.5} - \varepsilon_c}\right)^n\right)$$

The JMAK model is commonly used to describe any generic transformation within a material, and as such the broad assumptions do not necessarily reflect the transformation that occurs during DRX. However, establishing how the observed transformation deviates from the ideal model can provide insight into the phenomenological nature of the nucleation and growth mechanisms for DRX [31]. The original JMAK relationship assumes (i) pre-existing nuclei are randomly distributed throughout the volume, (ii) they form and isotropically grow at a constant rate (iii) until impingement occurs at which point a model correction should be implemented. Under these ideal assumptions, an Avrami exponent of $n = 4$ would be expected to describe the combined nucleation and growth kinetics of a material transformation. Refinements to the expected value for n can be made by recognizing physical factors about the dimensionality and controlling mechanisms for nucleation and growth [31]:

$$n = B + qd$$

B varies between 0 and 1 depending on whether nucleation is limited by site-saturation or expected to occur continuously at a constant rate, q defines the controlling mechanism for growth (0.5 for diffusion-controlled growth to 1.0 for interface-controlled growth), and d describes the dimensionality of growth (1D, 2D, 3D). As the nature of the uniaxial compression loading (2D, $d = 2$) with DRX (interface-controlled growth, $q = 1$) occurring at pre-existing grain boundaries of large grains (site-saturated, $B = 0$), an Avrami exponent on the order of $n = 2$ was expected. To model DRX, other considerations such as concurrent recovery and the decaying-nature of the driving force for recrystallized grain growth further act to lower n [32].

Avrami exponents were assessed by measuring the slope of a $\log\left(\ln\left(\frac{1}{1-X_v}\right)\right)$ by $\log\left(\frac{\varepsilon-\varepsilon_c}{\varepsilon_{0.5}-\varepsilon_c}\right)$ plot. For material hot-deformed 45–70 °C above $T_{\gamma'}$, n was measured as 1.4 for Co–9Al–9W–2Ta while $n = 1.5$ for Co–10Al–4W–25Ni–2Ta–2Ti. Although these values deviate from the expected theoretical value, they agree well with other experimentally determined exponents for DRX in structural metals [32]. For instance, hot working exponents of 1.5–1.8 have been reported for large-grain supersolvus Waspaloy [27, 40]. A variety of material factors may explain the apparent delay in supersolvus recrystallization kinetics of upset Co–Al–W alloys as compared to Waspaloy at similar temperatures relative to the γ' solvus. First, given similar grain size material was used in all studies, it is likely the presence of incoherent carbides in the commercial Waspaloy material provided additional recrystallization nuclei sites via particle-stimulated nucleation; no such particles exist in the Co–10Al–4W–25Ni–2Ta–2Ti alloy. Cellular automata simulations have confirmed the sensitivity of DRX transformation curves to additional nucleation sites, showing significant difference in behavior even with low volume fraction particles (0.04%) in large grain materials [41]. Second, it is likely high angle grain boundary migration during the growth stages, and likewise subgrain migration prior to recrystallization, is lower in the Co–Al–W-base alloy than in Waspaloy. High solute concentrations act as a drag on grain boundary migration. While the precise effect of a given alloying addition is dependent on the concentration and interaction with the boundary, larger atoms with low diffusivities, such as W, are more likely to increase the drag pressure and potentially contribute to the apparent delay in recrystallization.

Microstructure Evolution

Differences in DRX mechanisms at supersolvus temperatures were also observed between the two cobalt-base alloys investigated. While the hot compression flow curves suggest Co–9Al–9W–2Ta underwent discontinuous dynamic recrystallization at supersolvus temperatures, detailed characterization suggests DRX of the Co–10Al–4W–25Ni–2Ta–2Ti alloy occurred via strain-induced progressive lattice rotation. Distinct subgrains were observed throughout the non-recrystallized grains with increasing misorientation nearer pre-deformation high angle boundaries (Fig. 5). Characterization via TEM confirmed the sharp boundaries typically associated with subgrain, rather than cell, formation. Serrations on the size of these subgrains are frequently seen in the pre-deformation grain boundaries. Clear step changes in misorientation between neighboring subgrains were observed, with recrystallized grains defined when misorientations in excess of 15° were reached. This behavior is reminiscent of continuous dynamic recrystallization which is typically observed in materials with high stacking fault energies where dynamic recovery is very efficient [42], although the observed recrystallization occurred heterogeneously (predominantly at high angle grain boundaries and not homogeneously throughout the material).

Further, “copper-like” texture was consistently observed in the non-recrystallized grains at high reductions for both Co–Al–W-base alloys. In all cases, a strong [101] component was sometimes accompanied by a weaker [001] intensity; [111] fibers were completely absent in all cases (Fig. 6). While many microstructural factors influence texture development, the “copper-like” texture is also largely thought to be associated with medium-to-high SFE materials (a minor component around [111] would be expected to remain even after large strains in materials with low stacking

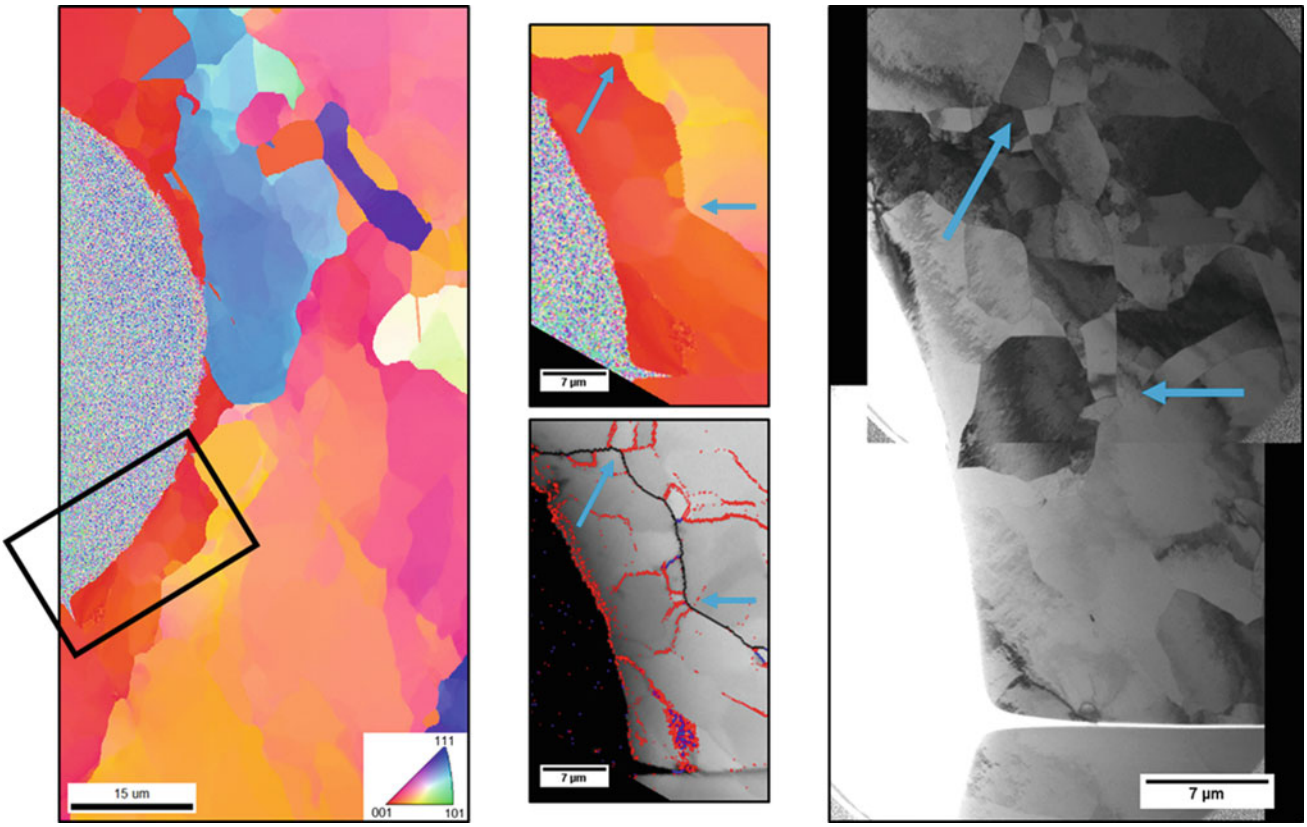

Fig. 5 (Right) Conventional bright field TEM montage illustrating cell and subgrain development in non-recrystallized grains of a Co–10Al–4W–25Ni–2Ta–2Ti specimen tested at 1182 °C, 0.01 s^{-1}, 1.46:1 reduction. TEM foil was cut from the center of the specimen along the bisection, parallel to compression direction. (Left, Upper Middle) IPF maps provide indication of neighboring region, with blue arrows pointing to consistent features in each of the maps. (Lower Middle) The grain boundary map indicates misorientations of 2°–5° (red), 5°–15° (blue), larger than 15° (black) as identified by TSL OIM Analysis software

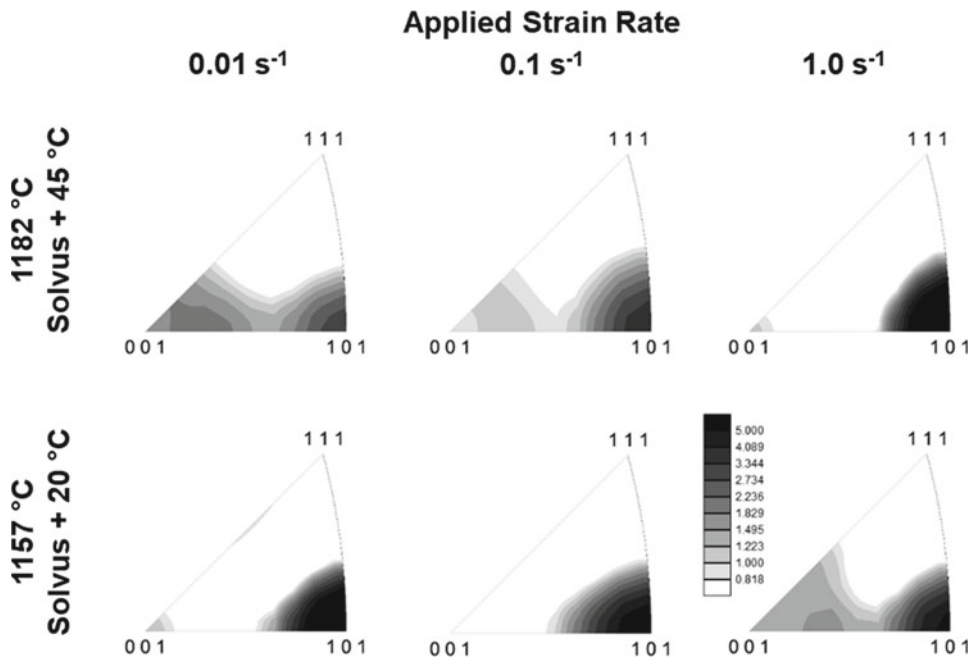

Fig. 6 Inverse pole figures showing non-recrystallized grain texture in Co–10Al–4W–25Ni–2Ta–2Ti relative to the compression direction after reduction at test conditions indicated

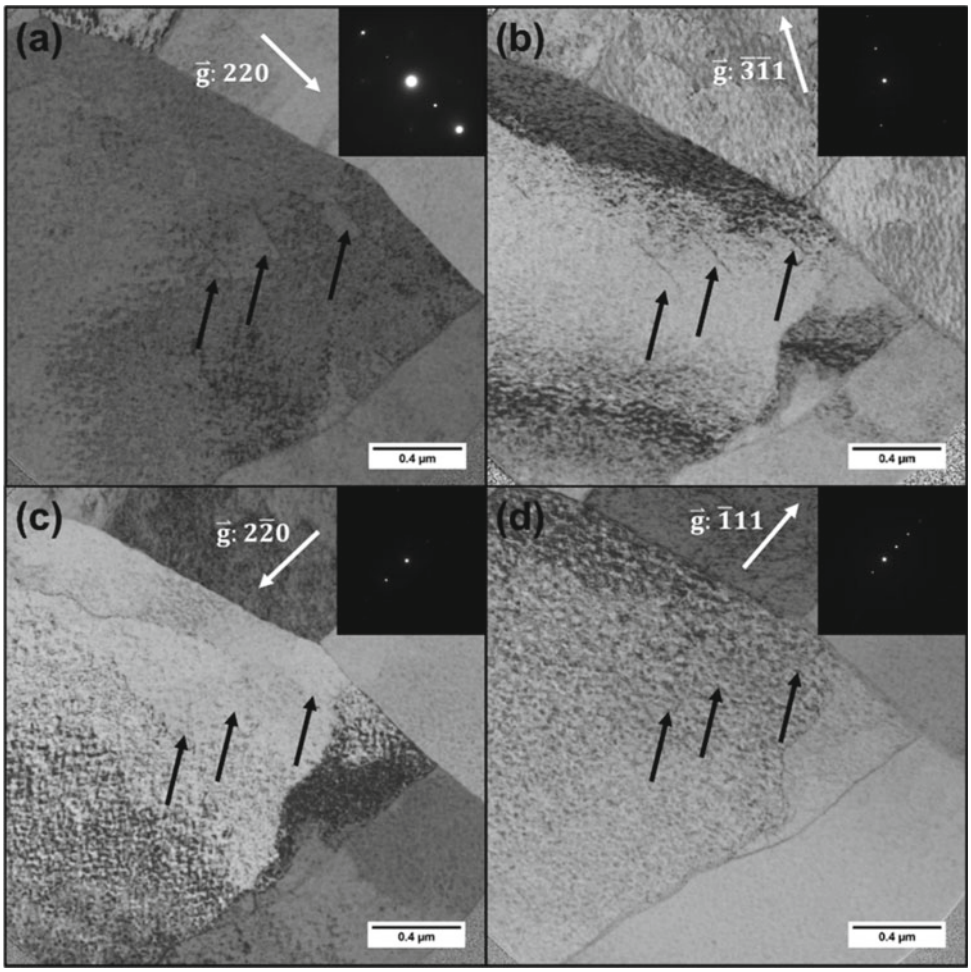

Fig. 7 Bright field TEM images showing slip-traces in Co–10Al–4W–25Ni–2Ta–2Ti compressed at 1182 °C, 0.01 s^{-1}. Near-screw dislocations with burgers vector a/2 [110] were **a**, **b** visible and **c**, **d** invisible under specific two-beam conditions near **a**, **c** (001) and **b**, **d** (112) zones. Intragranular contrast result of unsuppressed γ' formation upon water quenching after hot compression testing

fault energies) [32, 43]. While mixed octahedral and non-octahedral slip are expected for FCC systems at elevated hot working temperatures [44, 45]; the observed texture suggests large amounts of non-octahedral slip occurring, as with high stacking fault materials. Non-octahedral slip was confirmed in Co–10Al–4W–25Ni–2Ta–2Ti (Fig. 7).

Discussion

Results in Context of γ-FCC Stacking Fault Energy

While a number of microstructural factors influence the single-phase supersolvus hot deformation behavior of an FCC structural metal, the SFE along the octahedral {111} plane is the primary intrinsic material parameter controlling the response. When SFE is high, the equilibrium width between partial dislocations is small and recombination of partial dislocations into a single line is relatively easy, allowing the dislocation to cross-slip and climb. Due to the increased mobility, alloys with high SFE are more likely to experience dynamic recovery during deformation, reducing the level of stored energy in the deformed state and delaying DRX [46]. Materials with particularly high stacking fault energies, such as pure aluminum (166 mJ m^{-2}), undergo dynamic recovery as the principal restorative mechanism; DRX is typically not observed. Lower SFE materials have wider stacking faults, hindering cross-slip and climb, making dynamic recovery processes more difficult. Materials with lower stacking fault energies would be expected to have a higher level of stored work per unit strain with the increased dislocation density resulting in enhanced DRX. Comparison of the supersolvus deformation behavior of polycrystalline Co-Al-W-base alloys to that of conventional wrought nickel-base superalloys shows remarkably similar behavior given the room temperature SFE of FCC cobalt ($\sim$15 mJ m^{-2}) is an order of magnitude lower than elemental nickel ($\sim$128 mJ m^{-2}) [32, 46]. Even with considering the intermediate cobalt-nickel ratio for one of the compositions evaluated here, literature suggests the alloy stacking fault energy remains relatively low: SFE < 30 mJ m^{-2} for a (60–75 at %) Co–Ni alloy [46].

To better understand this apparent discrepancy, calculations using the axial nearest neighbor Ising model (ANNI)

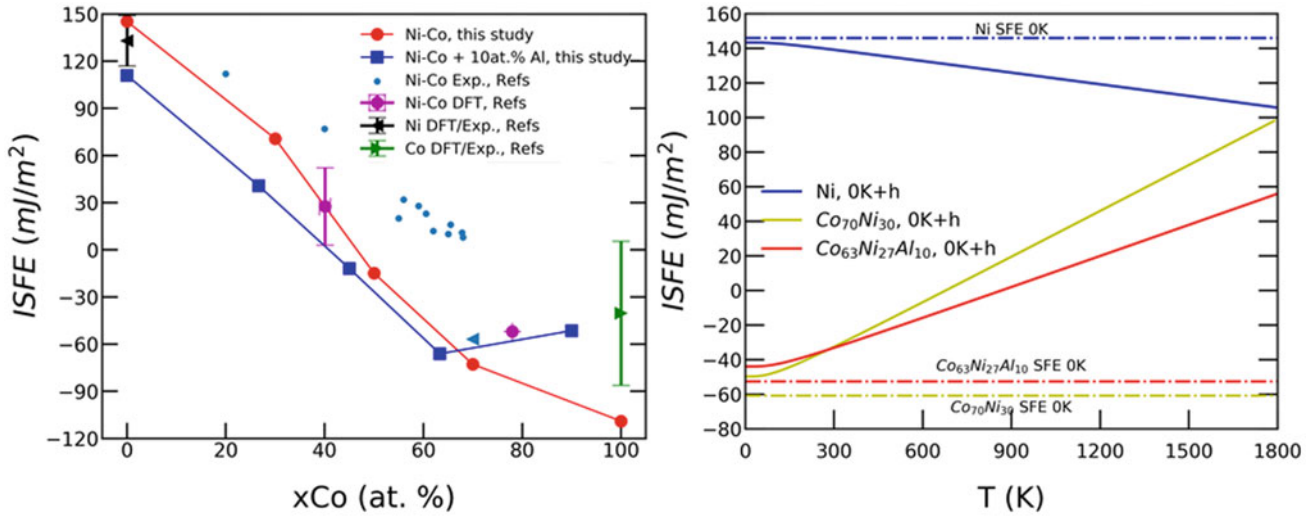

Fig. 8 **a** Density functional theory (DFT) calculations of Intrinsic Stacking Fault Energy (ISFE) at 0 K, with Ni–Co binary (red circles) and Ni–Co–Al (blue squares) from this analysis; other data points obtained from [11, 46, 48, 50, 51]; **b** Intrinsic stacking fault energies of Ni_{100}, $Co_{70}Ni_{30}$, and $Co_{63}Ni_{27}Al_{10}$ at elevated temperatures, as predicted with harmonic contributions

were employed to assess the SFE by evaluating the difference in energy between the HCP and FCC structures of the same composition [47]. Initial calculations examining the intrinsic stacking fault energy (ISFE) of the Ni–Co binary at 0 K were in good agreement with previously published simulations—increased Ni content increased the SFE of otherwise pure Co [48, 49]. The calculations here expand on those efforts to examine the compositional dependence of the Ni–Co–Al ternary in the Ni–Co-rich regions. At low temperatures, a small addition of Al (10 at.%) to the Co–Ni binary system was confirmed to lower the ISFE in Ni-rich compositions, but increase it in Co-rich compositions (Fig. 8a). Previous studies suggest tungsten additions likely act to also increase the ISFE relative to pure cobalt near 0 K [48]. However when harmonic approximations are considered in free energy estimates at hot working temperatures, the SFE of Ni_{100} and $Co_{70}Ni_{30}$ converge and Al alloying appears to lower the ISFE compared to Co–Ni with a similar atomic ratio (Fig. 8b). While the ISFE of more complex multi-component gamma phase Co–Al–W–(Ni)-base alloys at finite temperatures are difficult to calculate in the same manner; the findings here suggest the material property may not be as different as initially expected, supporting the finding of similar recrystallization kinetics between two-phase γ–γ' Ni–Al-base and Co–Al–W-base superalloys.

Conclusions

The similarity in hot working response between the investigated Co–Al–W-base alloys here and commercially available two-phase γ–γ' wrought nickel-base superalloys suggests contemporary supersolvus practices, presses, and tooling may be sufficient for aerospace component fabrication. Likewise, computational modeling tools for nickel-base alloys may be able to be leveraged to enable process—and location—specific simulation and microstructure optimization strategies; which could permit rapid transition or implementation of this novel alloy class:

- Flow behavior, apparent activation energy, and recrystallization kinetics agree well with reported values for a common conventional wrought γ–γ' Ni-base superalloy, Waspaloy.
- Hot worked material retained a magnetic field after processing, which led to challenges when handling and characterizing bulk material.
- Observed texture evolution and DRX kinetics are consistent with FCC materials of medium-to-high SFE.
- Progressive lattice rotation was identified as the predominant DRX mechanism for Co–Al–W-base alloys above solvus.
- Moderate Al additions were shown to raise the γ-FCC phase stacking fault energy considerably in the Co-rich region of the Ni–Co–Al ternary at room temperature, but appear to decrease SFE at hot working temperatures.

Acknowledgements The authors would like to acknowledge Mr. Pat Fagin, Mr. Joe Brown, and Mr. Travis Brown for the efficient processes and precise testing of the Co–Al–W-base alloys. This work was funded as part of internal efforts in the Metallic Materials and Processing Research Team of the Air Force Research Laboratory. SRN and MJM acknowledge the support of the National Science Foundation and the DMREF program under Grant 1922239. DW and MST further

acknowledge support of by the National Science Foundation under Grant DMR-1848128 and in part through computational resources provided by Information Technology at Purdue, West Lafayette, Indiana.

References

1. J. Sato, T. Omori, K. Oikawa, I. Ohnuma, R. Kainuma, and K. Ishida, "Cobalt-base high-temperature alloys," *Science*, vol. 312, no. 2006, pp. 90–91, 2006.
2. T. M. Pollock, J. Dibbern, M. Tsunekane, J. Zhu, and A. Suzuki, "New Co-based y-y' High-temperature alloys," *JOM*, vol. 62, no. 1, pp. 58–63, 2010.
3. A. Suzuki, H. Inui, and T. M. Pollock, "L12-Strengthened Cobalt-Base Superalloys," *Annu. Rev. Mater. Res.*, no. 45, pp. 345–68, 2015.
4. E. T. McDevitt, "Vacuum induction melting and vacuum arc remelting of Co-Al-W-X gamma-prime superalloys," *MATEC Web Conf.*, vol. 14, p. 02001, 2014.
5. E. T. McDevitt, "Feasibility of Cast and Wrought Co-Al-W-X Gamma-Prime Superalloys," *Mater. Sci. Forum*, vol. 783–786, pp. 1159–1164, 2014.
6. S. Neumeier, L. P. Freund, and M. Göken, "Novel wrought y/y' cobalt base superalloys with high strength and improved oxidation resistance," *Scr. Mater.*, vol. 109, pp. 104–107, 2015.
7. L. P. Freund, S. Giese, D. Schwimmer, H. W. Höppel, S. Neumeier, and M. Göken, "High temperature properties and fatigue strength of novel wrought γ-γ' Co-base superalloys," *J. Mater. Res.*, vol. 32, no. 24, pp. 4475–4482, 2017.
8. D. Weaver, "Thermomechanical Processing of a Gamma-Prime Strengthened Cobalt-Base Superalloy," PhD Thesis. The Ohio State University, 2018.
9. K. Wertz, "Exploration of Phase Stability and Hot Workability of Polycrystalline Co-Al-W-Base Superalloys," PhD Thesis. The Ohio State University, 2019.
10. P. Denteneer and W. Van Haeringen, "Stacking-fault energies in semiconductors from first-principles calculations," *J. Phys. C Solid State Phys.*, vol. 20, no. 32, p. L883, 1987.
11. M. Chandran and S. K. K. Sondhi, "First-Principle calculation of stacking fault energies in Ni- and Ni-Co Alloys," *J. Appl. Phys.*, vol. 109, no. 10, p. 103525, May 2011.
12. M. S. Titus, Y. M. Eggeler, A. Suzuki, and T. M. Pollock, "Creep-induced planar defects in L12-containing Co- and CoNi-base single-crystal superalloys," *Acta Mater.*, vol. 82, pp. 530–539, 2015.
13. A. Breidi, J. Allen, and A. Mottura, "First-principles calculations of thermodynamic properties and planar fault energies in Co_3X and Ni_3X $L1_2$ compounds: Thermodynamic properties and planar fault energies in Co3X and Ni3X," *Phys. status solidi*, vol. 254, no. 9, Sep. 2017.
14. A. Breidi, J. Allen, and A. Mottura, "First-principles modeling of superlattice intrinsic stacking fault energies in Ni3Al based alloys," *Acta Mater.*, vol. 145, pp. 97–108, Feb. 2018.
15. X. Zhang *et al.*, "Temperature dependence of the stacking-fault Gibbs energy for Al, Cu, and Ni," *Phys. Rev. B*, vol. 98, no. 22, p. 224106, Dec. 2018.
16. A. Zunger, S. H. Wei, L. G. Ferreira, and J. E. Bernard, "Special quasirandom structures," *Phys. Rev. Lett.*, vol. 65, no. 3, p. 353, 1990.
17. A. Van de Walle *et al.*, "Efficient stochastic generation of special quasirandom structures," *Calphad Comput. Coupling Phase Diagrams Thermochem.*, vol. 42, pp. 13–18, 2013.
18. G. Kresse and J. Furthmüller, "Efficient iterative schemes for ab initio total-energy calculations using a plane-wave basis set," *Phys. Rev. B*, vol. 54, no. 16, p. 11169, 1996.
19. J. Hafner, "Materials simulations using VASP—a quantum perspective to materials science," *Comput. Phys. Commun.*, vol. 177, no. 1–2, pp. 6–13, 2007.
20. P. E. Blöchl, "Projector augmented-wave method," *Phys. Rev. B*, vol. 50, no. 24, p. 17953, 1994.
21. J. P. Perdew, K. Burke, and M. Ernzerhof, "Generalized gradient approximation made simple," *Phys. Rev. Lett.*, vol. 77, no. 18, p. 3865, 1996.
22. H. J. Monkhorst and J. D. Pack, "Special points for Brillouin-zone integrations," *Phys. Rev. B*, vol. 13, no. 12, p. 5188, 1976.
23. M. Methfessel and A. Paxton, "High-precision sampling for Brillouin-zone integration in metals," *Phys. Rev. B*, vol. 40, no. 6, p. 3616, 1989.
24. L. Chaput, A. Togo, I. Tanaka, and G. Hug, "Phonon-phonon interactions in transition metals," *Phys. Rev. B*, vol. 84, p. 094302, 2011.
25. A. Togo and I. Tanaka, "First principles phonon calculations in materials science," *Scr. Mater.*, vol. 108, pp. 1–5, 2015.
26. A. Nicolay, G. Fiorucci, J. M. Franchet, J. Cormier, and N. Bozzolo, "Influence of strain rate on subsolvus dynamic and post-dynamic recrystallization kinetics of Inconel 718," *Acta Mater.*, vol. 174, pp. 406–417, 2019.
27. G. Shen, S. L. Semiatin, and R. Shivpuri, "Modeling microstructural development during the forging of Waspaloy," *Metall. Mater. Trans. A*, vol. 26, no. 7, pp. 1795–1803, 1995.
28. R. L. Goetz and V. Seetharaman, "Modeling Dynamic Recrystallization Using Cellular Automata," *Scr. Mater.*, vol. 38, no. 3, pp. 405–413, 1998.
29. A. Laasraoui and J. J. Jonas, "Prediction of Steel Flow Stresses at High Temperatures and Strain Rates," *Metall. Trans. A*, vol. 22, no. July, pp. 1545–1558, 1991.
30. G. Dieter, H. Kuhn, and S. L. Semiatin, *Handbook of Workability and Process Design*. 2003.
31. F. Montheillet and J. J. Jonas, "Models of Recrystallization," in *ASM Handbook, Vol. 22A: Fundamentals of Modeling for Metals Processing*, D. U. Furrer and S. L. Semiatin, Eds. 2009.
32. F. Humphreys and M. Hatherly, *Recrystallization and Related Annealing Phenomena*, Second. Pergamon, 2002.
33. D. S. Weaver and S. L. Semiatin, "Recrystallization and grain-growth behavior of a nickel-base superalloy during multi-hit deformation," *Scr. Mater.*, vol. 57, no. 11, pp. 1044–1047, 2007.
34. S. L. Semiatin *et al.*, "Deformation and recrystallization behavior during hot working of a coarse-grain, nickel-base superalloy ingot material," *Metall. Mater. Trans. A*, vol. 35, no. 2, pp. 679–693, 2004.
35. L. Briottet, J. J. JONAS, and F. Montheillet, "A Mechanical Interpretation of the Activation Energy of High Temperature Deformation in Two Phase Materials," *Acta Mater.*, vol. 44, no. 4, pp. 1665–1672, 1996.
36. K. I. Hirano, R. P. Agarwala, B. L. Averbach, and M. Cohen, "Diffusion in cobalt-nickel alloys," *J. Appl. Phys.*, vol. 33, no. 10, pp. 3049–3054, 1962.
37. S. Neumeier *et al.*, "Diffusion of solutes in fcc Cobalt investigated by diffusion couples and first principles kinetic Monte Carlo," *Acta Mater.*, vol. 106, pp. 304–312, 2016.
38. J. Favre, Y. Koizumi, A. Chiba, D. Fabregue, and E. Maire, "Recrystallization of L-605 cobalt superalloy during hot-working process," *TMS Annu. Meet.*, pp. 257–264, 2012.
39. A. Momeni, "The physical interpretation of the activation energy for hot deformation of Ni and Ni-30Cu alloys," *J. Mater. Res.*, pp. 1–8, 2016.

40. T. Matsui, "Dynamic Recrystallization Behavior of Waspaloy during Hot Working," *Mater. Trans.*, vol. 55, no. 2, pp. 255–263, 2014.
41. R. L. Goetz, "Particle stimulated nucleation during dynamic recrystallization using a cellular automata model," *Scr. Mater.*, vol. 52, no. 9, pp. 851–856, 2005.
42. S. Gourdet and F. Montheillet, "Materials Science and Engineering : A An experimental study of the recrystallization mechanism during hot deformation of aluminium," vol. 283, pp. 1–33, 2014.
43. H. Hu, "Texture of Metals," *Texture*, vol. 1, no. 4, pp. 233–258, 1974.
44. B. Bacroix and J. J. Jonas, "The Influence of Non-Octahedral Slip on Texture Development in FCC Metals," *Textures Microstruct.*, vol. 8,9, pp. 267–311, 1988.
45. D. Caillard and J. L. Martin, "Glide of dislocations in non-octahedral planes of fcc metals: A review," *Int. J. Mater. Res.*, vol. 100, no. 10, pp. 1403–1410, 2009.
46. P. C. J. Gallagher, "The influence of alloying, temperature, and related effects on the stacking fault energy," *Metall. Trans.*, vol. 1, no. 9, pp. 2429–2461, Sep. 1970.
47. P. J. . Denteneer and W. Van Haeringen, "Stacking-fault energies in semiconductors from first-principles calculations," *J. Phys. C Solid State Phys.*, vol. 20, no. 32, p. L883, 1987.
48. L. Y. Tian, R. Lizárraga, H. Larsson, E. Holmström, and L. Vitos, "A first principles study of the stacking fault energies for fcc Co-based binary alloys," *Acta Mater.*, vol. 136, pp. 215–223, 2017.
49. M. Chandran and S. K. Sondhi, "First-Principle calculation of stacking fault energies in Ni- and Ni-Co Alloys," *J. Appl. Phys.*, vol. 109, 2011.
50. T. Ericsson, "The temperature and concentration dependence of the stacking fault energy in the Co-Ni system," *Acta Metall.*, vol. 14, no. 7, pp. 853–865, Jul. 1966.
51. S. L. Shang, W. Wang, Y. Du, J. X. Zhang, A. . Patel, and Z. K. Liu, "Temperature-dependent ideal strength and stacking fault energy of FCC Ni: A first-principles study of shear deformation," *J Phys Condens Matter*, vol. 24, no. 15, 2012.